Journal of Thermal Engineering
https://jten.yildiz.edu.tr/
https://doi.org/10.47481/jten.0100

REVIEW ARTICLE

Computational analysis of micromagnetorotation on the concentration in a chemically reacting thermal process

M. S. Khan[1,*], N. H. Hajano[2], M. Fahad[3], F. A. Ixtiyarov[4]

[1]Department of Mathematics, Capital University of Science and Technology, 44000 Islamabad, Pakistan
[2]Department of Mathematics, Sukkur IBA University, 65200 Sukkur, Pakistan
[3]Department of Mathematics, Capital University of Science and Technology, 44000 Islamabad, Pakistan
[4]Center of Research and Innovation, Asia International University, 200103, Bukhara, Uzbekistan

Abstract

Understanding the coupled influence of magnetic fields and microrotation on heat and mass transfer in chemically reacting fluids is essential for the design of advanced cooling systems, polymer processing technologies, and biomedical transport devices. While previous studies have examined magneto-micropolar flows or chemically reacting transport processes independently, the combined effects of micromagnetorotation and chemical reactions in micropolar boundary layer flows remain largely unexplored. To address this gap, the present study develops a unified computational model for a chemically reacting micropolar boundary layer flow incorporating micromagnetorotation under a low Reynolds number approximation. The governing equations describing momentum, microrotation, temperature, magnetic induction, and species concentration are first reduced to a coupled system of nonlinear ordinary differential equations. These equations are then solved using the shooting method. The accuracy of the numerical procedure is verified through both step-size sensitivity and computational domain independence tests. The numerical results show that the thermal boundary layer becomes progressively thinner as the Prandtl number increases. For example, increasing the Prandtl number from 0.7 to 7 reduces the thermal boundary layer thickness by approximately 35%. A similar trend is observed for mass transport, where raising the Schmidt number from 0.6 to 2.0 decreases the concentration boundary layer thickness by nearly 40%. The magnetic Reynolds number has a noticeable influence on the flow, leading to higher fluid velocity as well as stronger magnetic induction, which reflects enhanced electromagnetic interaction between the fluid and the applied magnetic field. It is also found that increasing the magnetization parameter promotes microrotational motion, resulting in measurable changes in both the momentum and thermal fields. Unlike previous investigations, the present study examines the combined influence of micromagnetorotation and chemical reaction within a unified computational framework for micropolar boundary layer flow. This integrated analysis provides a clearer understanding of the interaction between magnetic effects, fluid microstructure, and reactive mass transport. The results demonstrate that micromagnetorotation not only modifies the concentration distribution but also affects the associated heat transfer characteristics. These findings may be useful for the design and optimization of engineering systems involving magnetically controlled heat and mass transfer, including biomedical transport processes and advanced manufacturing applications.

Keywords: Micropolar fluid, micromagnetorotation, chemically reacting boundary layer, magnetohydrodynamics (MHD), thermal and concentration fields

Cite this article as: Khan, M. S., Hajano, N. H., Fahad, M., & Ixtiyarov, F. A. (2026). Computational analysis of micromagnetorotation on the concentration in a chemically reacting thermal process. Journal of Thermal Engineering, 12(6), 2308–2321. https://doi.org/10.47481/jten.0100

1. Introduction

The influence of micromagnetorotation (MMR) on magnetohydrodynamic (MHD) micropolar flows has recently received substantial attention due to its significant implications in transport phenomena, energy conversion, and biofluid dynamics [1]. The interaction between microrotation and magnetic fields has been shown to strongly change velocity, temperature, and concentration distributions, making it an active topic in both theoretical and applied research [2]. Khan and

*Corresponding Author
E-mail Adress: muhammad.sabeel@cust.edu.pk

Submitted: 22 October 2025; **Accepted:** 19 April 2026

This paper was recommended for publication in revised form by Editor-in-Chief Ahmet Selim Dalkılıç

Published by Yıldız Technical University, İstanbul, Türkiye

Hameed [3] introduced a new magneto-micropolar boundary layer model emphasizing the role of micromagnetorotation in altering the momentum and energy transport mechanisms. Their study proved that the inclusion of induced magnetic fields produces noticeable deviations from the conventional magneto-micropolar model. The results showed that magnetic induction alters both the velocity and temperature distributions, emphasizing the importance of considering these effects in electrically conducting micropolar fluids. Building on this work, Khan and Hameed [4] used the FreeFEM++ finite element platform to examine heat transfer in electrically induced micropolar flows. Their numerical results showed that micromagnetorotation (MMR) enhances heat transfer while also influencing the overall stability of the flow. Aslani et al. [5] provided one of the first detailed analyses of micromagnetorotation in MHD micropolar flows, where they found that MMR could serve as a key parameter controlling hydrodynamic stability. Later, Aslani and Sarris [6] extended this work to magnetohydrodynamic Poiseuille micropolar flows, providing analytical solutions and stability criteria. More recently, Aslani et al. [7] explored the mechanics of conducting micropolar fluids having magnetic particles, showing that the vorticity-microrotation difference under MMR can be an important measure of energy transfer in electrically conducting suspensions.

The thermal and boundary layer consequences of MMR have been studied by multiple groups. Khan [8] developed a thermal boundary layer model that incorporates micromagnetorotation and proved that regulating the boundary layer thickness can significantly improve thermal performance. Baithaiah and Mishra [9] investigated free-convection magneto-micropolar flow through porous media and found that micromagnetorotation enhances energy transport while improving the stability of buoyancy-driven flows. Recent research has also highlighted the growing use of artificial neural networks (ANNs) in conjunction with classical numerical methods for solving nonlinear transport problems. Hybrid Runge-Kutta-ANN techniques have been successfully applied to chemically reacting micropolar boundary layer flows, providing reliable predictions of velocity, temperature, microrotation, and concentration distributions [10]. Similar machine-learning approaches have been employed to model hybrid nanofluids in porous and magnetized media for improved thermal regulation and heat transfer prediction [11]. Other studies have examined chemically reacting MHD boundary layer flows over curved stretching surfaces, emphasizing the influence of partial slip, viscous dissipation, and non-uniform heat generation on transport characteristics relevant to industrial applications [12]. ANN-based models have likewise been used to investigate nanofluid flow in parabolic trough solar collectors for enhanced thermal management [13], to evaluate the combined effects of nanoparticle aggregation and thermal radiation in chemically reacting systems [14], and to predict heat and mass transfer in microchannel nanofluid flows having microorganisms [15]. In addition, entropy generation and mass transfer in rotating magnetized flows with chemical reactions have been explored with the aim of improving heat dissipation and the operating efficiency of compact thermal systems [16,17].

Several studies have examined the sensitivity of micropolar flows to the governing physical parameters. Tian et al. [18] carried out an optimization and sensitivity analysis and showed that both micromagnetorotation (MMR) and thermal-magnetic coupling have a pronounced effect on concentration transport. Similar observations were reported by Hameed and Khan [19], who numerically investigated electrically conducting micropolar fluids and proved that MMR significantly alters the rheological behavior as well as the associated transport characteristics. The interaction between magnetic fields and micropolar fluids has also been the subject of considerable research. Eringen's pioneering [20] set up the theoretical foundation for magnetohydrodynamic and electrodynamic effects in micropolar fluids, offering important insight into the influence of magnetic fields on fluid microstructure. More recently, Reddy et al. [21] investigated MHD nanofluid stagnation-point flow over a stretching sheet and highlighted the role of magnetic induction in changing the flow behavior. Micropolar fluid theory has found widespread application in modeling complex fluids such as blood, liquid crystals, colloidal suspensions, and non-Newtonian lubricants [22]. For example, Karvelas et al. [23] proved that increasing microrotation and vortex viscosity leads to a noticeable reduction in wall shear stress, emphasizing the importance of microstructural effects in predicting the rheological response of such fluids. Almakki et al. [24] proposed a micropolar nanofluid model for MHD unsteady flow with entropy generation occurring through a stretched surface at the boundary. Khan et al. [25] employed a finite element approach to investigate MHD micropolar flow in a rectangular channel. Their numerical results showed that increasing the micropolar coupling parameter suppresses both magnetic induction and the microrotational velocity of suspended particles. In a related study, Khan and Hameed further explored heat transfer characteristics in MHD micropolar flows, offering added insight into the interaction between magnetic fields, fluid motion, and thermal transport. The influence of micromagnetorotation has also been examined in entropy generation and transport phenomena. Ismael et al. [26] reported that the presence of MMR alters entropy production and affects the second-law efficiency of micropolar nanofluids having nanoparticles. Likewise, Pang and Srivastava [27] investigated double-diffusive instabilities in micropolar fluids and found that micromagnetorotation promotes both thermal and solutal diffusion, making it relevant to a variety of geophysical and industrial applications [28]. Beyond these fundamental studies, MMR has attracted increasing attention in biomedical engineering and microfluidic systems. Aslani et al. [29] analyzed micropolar flow through micro-conductors and proved that micromagnetorotation can be used to regulate biofluid transport, including oscillatory blood flow in stenosed arteries. Their findings also suggested that induced microrotation offers an effective mechanism for controlling heat transfer in complex engineering systems. Recent investigations have further emphasized the importance of flow configuration and magnetic effects in thermal transport. Numerical studies of nanofluid-based thermal systems have shown that changing the flow geometry can substantially improve heat and mass transfer rates [30]. Similarly, three-dimensional computational analyses have proved that geometric optimization plays a significant role in enhancing thermal efficiency [31], while twisted and helical flow configurations have been reported to improve thermal-hydraulic performance, particularly in low-Reynolds-number regimes [32]. Other studies have shown that non-uniform magnetic fields can significantly change heat transfer through magnetization effects [33], while simulations of rotational and swirling flows show that enhanced mixing promotes more effective thermal transport [34]. These observations further justify investigating the combined influence of microrotation and magnetic induction on chemically reacting micropolar boundary layer flows.

The studies discussed above clearly prove that micromagnetorotation has an important influence on flow behavior, heat transfer, and mass transport in micropolar fluids. Despite these advances, the simultaneous consideration of micromagnetorotation and chemical reaction effects in micropolar boundary layer flows stays largely unexplored. Existing investigations have generally focused either on magneto-micropolar flow or on chemically reacting transport processes, without accounting for the coupled interaction among magnetic induction, microrotational motion, and reactive species transport. To address this limitation, the present work investigates a chemically reacting micropolar boundary layer flow in the presence of micromagnetorotation under the low-Reynolds-number approximation. A unified mathematical model is formulated to capture the coupled transport mechanisms governing momentum, microrotation, heat, and species concentration. The resulting nonlinear ordinary differential equations are solved numerically using the shooting method, providing a framework for examining the combined effects of magnetic induction and chemical reaction on the transport characteristics of micropolar fluids.

The present study makes several contributions to the analysis of chemically reacting micropolar boundary layer flows under the influence of micromagnetorotation. The proposed model combines magnetic induction, microrotational effects, and chemical reactions within a single mathematical framework, allowing their coupled influence on transport phenomena to be examined in a consistent manner. The resulting nonlinear boundary value problem is solved numerically using a shooting method, and the numerical implementation is verified to ensure the reliability of the computed solutions. Attention is given to the influence of governing dimensionless parameters. The effects of the Prandtl number, Schmidt number, magnetic Reynolds number, magnetization parameter, and micropolar coupling parameter are investigated to understand how each parameter changes the velocity, microrotation, temperature, magnetic induction, and concentration distributions. The distinguishing feature of the present work is the simultaneous treatment of micromagnetorotation and chemical reaction effects within a unified computational framework. This combined analysis provides a more comprehensive description of reactive transport in micropolar fluids than approaches that consider these mechanisms separately. This coupled analysis offers new physical insights into magnetically controlled reactive transport mechanisms and extends the applicability of micropolar boundary layer theory to advanced engineering and biomedical systems.

The rest of the paper is organized as follows. In Section 2 physical description of the problem is described along with the mathematical model governing the flow dynamics of the considered problem. In Section 3, the numerical solution method is said to solve the flow model problem. In Section 4, the results obtained are discussed in detail. Finally, conclusions are drawn in Section 5.

2. Physical description of the model problem and mathematical model

We consider the steady two-dimensional boundary layer flow of a micropolar fluid under the influence of magnetohydrodynamic (MHD) convection and an externally applied magnetic field. A Cartesian coordinate system is adopted, where the x-axis is taken along the direction of the free-stream flow and the y-axis is measured normally to the surface. As the fluid moves over the surface, velocity, temperature, concentration, and microrotation boundary layers develop simultaneously, and their interactions decide the overall transport characteristics of the flow. The physical setup along with the coordinate

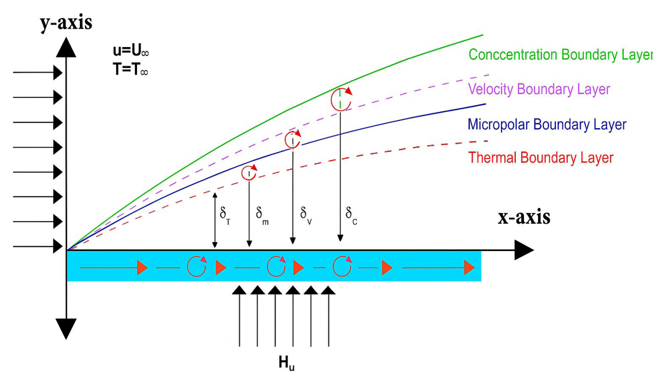

Figure 1. Geometric description of the model system is depicted in the Figure 1. The vector form of the governing equations is as follows [35].

$$\nabla \cdot U = 0, \tag{1}$$

$$\nabla \cdot H = 0, \tag{2}$$

$$\rho \frac{dU}{dt} + U \cdot \nabla U + \nabla p = \eta \nabla^2 U + 2\eta \nabla \times (W - w) + (\nabla \times H) \times B + (M \cdot \nabla) H + M \times (\nabla \times H), \tag{3}$$

$$\rho \frac{dH}{dt} + U \cdot \nabla H = \eta \nabla^2 H + H \cdot \nabla U, \tag{4}$$

$$I \frac{dW}{dt} = \gamma \nabla^2 W + 4\eta (w - W) + M \times H - U \cdot \nabla W, \tag{5}$$

$$\frac{dT}{dt} + \frac{Q}{\rho c_p}(T - T_\infty) + \frac{1}{\rho c_p} \nabla \cdot (0, q_r) = U \cdot \nabla T - \kappa \Delta T, \tag{6}$$

$$\frac{dC}{dt} + D\Delta C = U \cdot \nabla C, \tag{7}$$

$$B - M = \mu_0 H, \tag{8}$$

$$M = M_0 (I - \tau W \cdot \epsilon), \tag{9}$$

$$J = \sigma (E + U \times B). \tag{10}$$

In this context, the variables are defined as, ρ denotes the fluid density, p represents the pressure, is the current density, l is the moment of inertia, μ_0 is the magnetic permeability, σ is the electrical conductivity, B refers to the magnetic induction vector, η is the shear viscosity, η_1 is the vortex viscosity, γ is the angular viscosity, $M \times H$ describes the MMR effect, which accounts for how magnetization influences microrotation. D, κ, Q, and q_r are molecular diffusivity, thermal diffusivity, dimensional heat source, and radiative heat flux, respectively.

2.1. Component form of the governing equations

The component form of the model is obtained under the following assumptions for the flow field variables: $U = (u(x, y), 0, 0)^t$, $\omega = (0, 0, \omega(x, y))^t$, $H = (0, H_0, 0)^t$, and $W = (0, 0, \Omega(x, y))^t$. Following the vector-tensor calculus (see Appendix A in [8]), the part form of the governing equations (1)-(10) is obtained as follows.

$$\frac{\partial u}{\partial x} + \frac{\partial v}{\partial y} = 0, \tag{11}$$

$$u\frac{\partial u}{\partial x} + v\frac{\partial u}{\partial y} = (\mu + k)\frac{1}{\rho}\frac{\partial^2 u}{\partial y^2} - \frac{\sigma}{\rho}\mu_0 H_2^2 u + \frac{k}{\rho}\frac{\partial N}{\partial y} + \frac{1}{\rho M_0 \widehat{H}}(H_1 + \tau N H_2)\frac{\partial H_1}{\partial x} + (H_2 - \tau N H_1)\frac{\partial H_2}{\partial x}, \tag{12}$$

$$u\frac{\partial H_1}{\partial x} + v\frac{\partial H_1}{\partial y} = H_1\frac{\partial u}{\partial x} + H_2\frac{\partial u}{\partial y} + \mu_0\frac{\partial^2 H_1}{\partial y^2} \tag{13}$$

$$H_0 M_0 \tau N + \frac{k}{\rho_j}\left(2N + \frac{\partial u}{\partial y}\right) = u\frac{\partial N}{\partial x} + v\frac{\partial N}{\partial y} - \frac{\gamma^*}{\rho_j}\frac{\partial^2 N}{\partial y^2}, \tag{14}$$

$$\frac{Q}{\rho c_p}(T - T_\infty) + \frac{1}{\rho c_p}\frac{\partial q_r}{\partial y} = u\frac{\partial T}{\partial x} + v\frac{\partial T}{\partial y} - \kappa\frac{\partial^2 T}{\partial y^2}, \tag{15}$$

and

$$D\frac{\partial^2 C}{\partial y^2} = u\frac{\partial C}{\partial x} + v\frac{\partial C}{\partial y}. \tag{16}$$

The system in Eqs. (11)-(16) is subjected to the following boundary conditions.

$$u = \alpha x,\ v = 0,\ N = -N_0\frac{\partial u}{\partial y},\ \frac{\partial H_1}{\partial y} = 0,\ H_2 = 0,\ \text{at } y = 0,$$
$$T = T_w,\ C = C_w,\ u \to ax,\ H_1 \to H_0 x,\ N \to 0,\ T \to T_\infty,\ C \to C_\infty \ \text{as } y \to \infty$$

2.2. Non-dimesionalization

The mathematical model in Eqs. (11)-(17) is transformed into a system of ordinary differential equations (ODEs) using the following similarity transformations.

$$\begin{cases} v = -\sqrt{\nu c}\, f(\eta), \\ u = x f'(\eta) c, \\ \eta = \sqrt{\frac{c}{\nu}}\, y, \\ N = c\alpha\sqrt{\frac{c}{\nu}}\, g(\eta), \\ H_1 = H_0 \alpha h'(\eta), \\ H_2 = -h(\eta) \cdot H_0\sqrt{\frac{\nu}{c}}. \end{cases} \tag{18}$$

$$T = T_\infty - (T_w - T_\infty)\theta(\eta),\ T^4 = 4T_\infty^3 T - 3T_\infty^4,\ C = C_\infty + C_0 x \phi(\eta). \tag{19}$$

The transformations in Eqs. (18) and (19) when applied to Eqs. (11)-(17) lead to the following system.

$$(1 + K) f''' = f'^2 - ff'' - \alpha h'^2 + \left(\frac{R_m}{R_e}\right) h^2 f' - Kg' + \omega g h h', \tag{20}$$

$$\lambda h''' = hf'' - h''f, \tag{21}$$

$$\left(1 + \frac{K}{2}\right) g'' = \beta^* (2g + f'') - f'g - \frac{\omega}{\alpha} g - fg', \tag{22}$$

$$\frac{\left(1 + \frac{4}{3}R\right)}{Pr}\theta'' + f\theta' + S\theta = 0, \tag{23}$$

and

$$\phi'' = S_c (f'\phi - f\phi'). \tag{24}$$

along with the boundary conditions

$$\phi(0) = 1,\ \theta(0) = 1,\ f = 0,\ f' = 1,\ h = 0,\ g = -N_0 f'',\ h'' = 0,\ \text{at } \eta = 0 \tag{25}$$

and

$$f' = \frac{a}{c},\ h' = 1,\ g = 0,\ \phi(\infty) = 0,\ \theta(\infty) = 0,\ \text{at } \eta \to \infty \tag{26}$$

The physical significance of the imposed boundary conditions is as follows. At the surface ($\eta = 0$), the condition $f = 0$ and $f' = 1$ is the no-slip and stretching velocity of the surface, showing that the fluid adheres to the boundary and moves with the wall velocity. The condition $\theta(0) = 1$ and $\phi(0) = 1$ correspond to prescribed wall temperature and concentration, respectively, ensuring that heat and mass transfer originate from the surface. The microrotation condition $g = -N_0 f''$ is a proportional relationship between microrotation and the shear at the wall, which is characteristic of micropolar fluids. The magnetic condition $h = 0$ and $h'' = 0$ imply that the induced magnetic field satisfies the boundary constraints at the surface. Far from the surface ($\eta \to \infty$), the condition $f' \to \frac{a}{c}$ is the free stream velocity, showing that the flow approaches the ambient state. The conditions $\theta(\infty) = 0$ and $\phi(\infty) = 0$ imply that temperature and concentration approach their ambient values, ensuring proper decay of thermal and concentration boundary layers. The condition $g \to 0$ shows that microrotation effects vanish far from the surface, while $h' \to 1$ ensures that the magnetic field approaches the applied external magnetic field. These boundary conditions collectively ensure a physically consistent description of the flow, thermal, and concentration fields within the boundary layer.

In Eqs. (20)-(24), the dimensionless parameters are said as follows.

$$K = \frac{k}{\mu},\ \frac{R_m}{R_e} = \frac{\sigma H_0^2 \nu}{\rho c^2},\ R_m = \sigma\mu\mu_0\nu_0 L,\ R_e = \frac{\nu_0 L}{\nu},\ d = \frac{H_0^2}{c^2 l},\ \lambda = \frac{\mu_0}{\nu},$$
$$\left(1 + \frac{k}{2}\right) = \frac{\gamma^*}{\rho_j},\ \frac{\omega}{\alpha} = \frac{\tau M_0 \mu_0 \bar{H}}{c},\ \text{and}\ \ \omega = \frac{\tau M_0 H_0^2}{\rho \bar{H} c}.$$

The skin friction coefficient denoted C_f and is defined as

$$C_f = \frac{\tau_w}{\rho u_w^2},$$

where, $u_w = cx$ is the characteristic velocity, and τ_w is the wall shear stress given by

$$\tau_w = \left[(\mu + k)\frac{\partial u}{\partial y} + kN\right]_{y=0}.$$

Substituting Eq. (30) into Eq. (29) gives skin-friction coefficient in the following form.

$$(1 + K)f''(0) + Kg(0) = C_f\sqrt{R_{ex}},$$

where $Re_x = u_w x/\nu$ is the local Reynolds number.

2.3. Model assumptions and limitations

The present mathematical model is developed under several simplifying assumptions to ensure tractability while capturing the essential physics of the problem. First, the flow is assumed to be two-dimensional, steady, and laminar, which is valid for boundary layer flows at low to moderate Reynolds numbers. Second, a low magnetic Reynolds number approximation is employed, implying that the induced magnetic field is small compared to the applied magnetic field; therefore, magnetic induction effects are simplified. Third, the fluid is modeled as a micropolar fluid, which accounts for microstructural effects such as particle rotation, but assumes a homogeneous and isotropic medium.

The chemical reaction is assumed to follow first-order kinetics with a constant reaction rate. Thermal radiation is treated using a linearized approximation, which is valid for small temperature differences within the boundary layer. In addition, viscous dissipation, Joule heating, and buoyancy effects are neglected to focus on the dominant micromagnetorotation and reactive transport mechanisms.

These assumptions define the scope of the present study and ensure mathematical and computational feasibility. The present formulation is developed under several simplifying assumptions and is therefore most suitable for laminar flows with relatively simple reaction mechanisms. Problems involving turbulence, very strong magnetic fields, or multistep chemical reactions require added modeling. Extending the current framework to include nonlinear radiation, higher-order reaction kinetics, and turbulence would make the model applicable to a wider range of engineering and biomedical transport problems.

3. Method of solution

The coupled nonlinear ordinary differential equations are solved numerically using the shooting method. Since the governing equations are of higher order, they are first rewritten as an equivalent system of first-order differential equations, making them suitable for numerical integration. The boundary value problem is then converted into an initial value problem by assigning initial estimates for the unknown boundary conditions. These estimates are refined iteratively until the prescribed boundary conditions at the far-field boundary are satisfied. During each iteration, the resulting system of first-order equations is integrated using the fourth-order Runge-Kutta method. Through this process, the solution is progressively refined until convergence is achieved. The numerical integration is carried out using a fourth-order Runge-Kutta scheme with a sufficiently small step size to ensure numerical stability. Convergence of the shooting procedure is achieved through Newtons iterative method, which provides rapid and stable convergence for the present nonlinear boundary value problem.

To apply shooting method, we first transform the boundary value problem in Eqs. (20)-(24) to first order ODE system with the following substitutions. Let

$$\begin{aligned}
&f(\eta) = Z_1,\ f'(\eta) = Z_2,\ f''(\eta) = Z_3,\ f'''(\eta) = Z_3',\\
&h(\eta) = Z_4,\ h'(\eta) = Z_5,\ h''(\eta) = Z_6,\ h'''(\eta) = Z_6',\\
&g(\eta) = Z_7,\ g'(\eta) = Z_8,\ g''(\eta) = Z_8',\theta(\eta) = Z_9,\\
&\theta'(\eta) = Z_{10},\ \theta''(\eta) = Z_{10}',\phi(\eta) = Z_{11},\\
&\phi'(\eta) = Z_{12},\ \phi''(\eta) = Z_{12}'.
\end{aligned} \tag{31}$$

The transformed system thus becomes

along with the boundary conditions at infinity as

$$\begin{aligned}
&Z_1' = Z_2, && Z_1(0) = 0,\\
&Z_2' = Z_3, && Z_2(0) = 1,\\
&Z_3' = \frac{1}{1+K}\left[\left(\frac{R_m}{R_e}\right)Z_4^2 Z_2 - KZ_8 - \alpha Z_5^2 + \omega Z_7 Z_4 Z_5 + Z_2^2 - Z_1 Z_3\right], && Z_3(0) = p,\\
&Z_4' = Z_5, && Z_4(0) = 0,\\
&Z_5' = Z_6, && Z_5(0) = q,\\
&Z_6' = \frac{1}{\lambda}(Z_4 Z_3 - Z_6 Z_1), && Z_6(0) = 0,\\
&Z_7' = Z_8, && Z_7(0) = -N_0 p,\\
&Z_8' = \frac{2}{2+K}\left[\beta^*(2Z_7 + Z_3) - \frac{\omega}{\alpha}Z_7 + Z_2 Z_7 - Z_1 Z_8\right], && Z_8(0) = r,\\
&Z_9' = Z_{10}, && Z_9(0) = 1,\\
&Z_{10}' = -\frac{3}{3+4R}P_r(Z_1 Z_{10} + SZ_9), && Z_{10}(0) = s,\\
&Z_{11}' = Z_{12}, && Z_{11}(0) = 1,\\
&Z_{12}' = S_c(Z_2 Z_{11} - Z_1 Z_{12}), && Z_{12}(0) = t.
\end{aligned}$$

$$\left.\begin{array}{l} Z_2(\eta_\infty) = \frac{a}{c}, \\ Z_5(\eta_\infty) = 1, \\ Z_7(\eta_\infty) = 0, \\ Z_9(\eta_\infty) = 0, \\ Z_{11}(\eta_\infty) = 0. \end{array}\right\} \quad (32)$$

In practical computations, the boundary at infinity is approximated by a sufficiently large finite value of η_∞, beyond which further increases do not alter the solution profiles, ensuring numerical consistency. To solve this system, Newton's method is used with the following update rule.

$$\begin{bmatrix} p^{n+1} \\ q^{n+1} \\ r^{n+1} \\ s^{n+1} \\ t^{n+1} \end{bmatrix} = \begin{bmatrix} p^{n} \\ q^{n} \\ r^{n} \\ s^{n} \\ t^{n} \end{bmatrix} - \begin{bmatrix} Z_{13} & Z_{14} & Z_{15} \\ Z_{18} & Z_{19} & Z_{20} \\ Z_{23} & Z_{24} & Z_{25} \end{bmatrix}^{-1} \cdot \begin{bmatrix} Z_2 - \frac{a}{c} \\ Z_5 - 1 \\ Z_7 \\ Z_9 \\ Z_{11} \end{bmatrix} \quad (33)$$

The convergence criterion in the present numerical scheme is defined by the largest absolute residual of the boundary conditions imposed at infinity. Specifically, convergence is achieved when

$$\max\left\{\left|Z_2 - \frac{a}{c}\right|, |Z_5 - 1|, |Z_7|, |Z_9|, |Z_{11}|\right\}\text{\lt}\epsilon \quad (34)$$

where the tolerance is set to $\epsilon = 10^{-10}$. This stringent tolerance ensures numerical stability, accuracy, and consistency of the computed solutions. The iterative procedure is continued until all residuals simultaneously satisfy this criterion.

Alternative numerical approaches, such as finite difference and finite element methods, can also be considered for solving the present boundary value problem. However, the shooting method combined with the Runge-Kutta scheme was preferred due to its computational efficiency, ease of implementation, and proven accuracy for smooth boundary layer flows. The method transforms the boundary value problem into an equivalent first value problem, allowing the use of highly correct and stable integration techniques. The Newton iteration shows quadratic convergence, ensuring rapid and reliable determination of the unknown first conditions, while the fourth-order Runge-Kutta scheme guarantees high accuracy in numerical integration. Furthermore, compared to grid-based methods, the shooting technique avoids the formation of large system matrices, thereby reducing computational complexity and improving efficiency for the present system of coupled nonlinear equations.

4. Validation of the numerical solution

To confirm the present numerical solution, a limiting case of the model was compared with results reported in the literature. By neglecting the concentration and thermal energy equations, the present model reduces to the benchmark micropolar boundary layer flow studied by Isma and Khan [19], where the governing equations and skin-friction coefficient $C_f\sqrt{Re_x}$ were analyzed under similar parametric conditions. Numerical values of the skin-friction coefficient for different values of the material parameter λ with varying microrotation parameter α and $\omega\omega^* = 0.1$ were extracted from Table 1 of [19] and compared with the corresponding results obtained from the reduced form of the present model. The present results closely match the reference data, with the percentage error staying below 0.001% in all cases. The errors are computed by

$$\text{Error}(\%) = \left|\frac{C_f\sqrt{Re_x}^{\text{Present}} - C_f\sqrt{Re_x}^{\text{Reference}}}{C_f\sqrt{Re_x}^{\text{Reference}}}\right| \times 100$$

It is clear from Table 1 that the present results are in excellent agreement with those reported by Isma and Khan [19], thereby confirming the numerical method employed. A grid-independence and tolerance-sensitivity analysis was performed and shown in Table 2 to ensure the accuracy and reliability of the numerical solution. Since the present problem is reduced to a system of ordinary differential equations in the similarity variable η, grid independence is examined in terms of step-size (Δη) and computational domain truncation (η_{max}). The governing equations were solved using progressively smaller step sizes, and the resulting values of key physical quantity such as $C_f\sqrt{Re_x}$ was checked. It was seen that reducing the step size below $\Delta\eta = 0.005$ produced negligible changes in the computed results, confirming grid independence.

Table 1. Comparison of the skin-friction coefficient $C_f\sqrt{Re_x}$ for different values of the material parameter

λ with varying microrotation parameter α at $\omega\omega^* = 0.1$, and K = 1.

λ	α	$C_f\sqrt{Re_x}$ [19]	Present Results	Error (%)
0.5	0.3	1.04161082758066	1.04161115	0.00003
	0.5	0.865391704012286	0.86539212	0.00005
	0.9	0.323381942307113	0.32338245	0.00015
2.5	0.3	1.01390953667492	1.01391087	0.00013
	0.5	0.824727180237149	0.82472764	0.00006
	0.9	0.274956992554628	0.27495810	0.00041
5.0	0.3	0.990595668409694	0.99059632	0.00007
	0.5	0.778325579855818	0.77832611	0.00007
	0.9	0.230118058368731	0.23011945	0.00059

Similarly, the far-field boundary condition at $(\eta \to \infty)$ was approximated by selecting a sufficiently large finite value of η_{max}. Numerical experiments showed that η_{max} = 10-15 is adequate for all flow variables, beyond which further increases do not affect the solution profiles, thereby ensuring domain independence. In addition, tolerance sensitivity of the shooting method was examined by varying the convergence criterion given below.

$$\max\left\{\left|f'(\eta_{max}) - \frac{a}{c}\right|, |h'(\eta_{max}) - 1|, |g(\eta_{max})|, |\theta(\eta_{max})|, |\phi(\eta_{max})|\right\} < 10^{-6} \quad (35)$$

It was found that reducing the tolerance below 10^{-6} does not significantly alter the numerical results, showing that the solution is stable and insensitive to further tightening of the convergence criterion. In the present computations, a stricter tolerance of $\epsilon = 10^{-10}$ is employed to ensure high accuracy and numerical consistency.

Table 2. grid independence study for skin-friction coefficient $C_f\sqrt{Re_x}$ at $\lambda = 2.5$, $\alpha = 0.5$, $K = 1$, $\omega\omega^* = 0.1$,

$Pr = 1$, and $Sc = 1$.

$\Delta\eta$	η_{max}	$C_f\sqrt{Re_x}$	Error (%)
0.02	10	−0.82472184	0.00070
0.01	10	−0.82472593	0.00021
0.005	10	−0.82472718	0.00000
0.0025	10	−0.82472719	0.00001

5. Results and discussion

During the transformation of the governing partial differential equations (PDEs) into a system of ODEs, several physical parameters appear. The effects of these parameters on the hydrodynamic velocity, microrotational velocity, magnetic induction, temperature distribution, and concentration profile are carefully studied using graphical results.

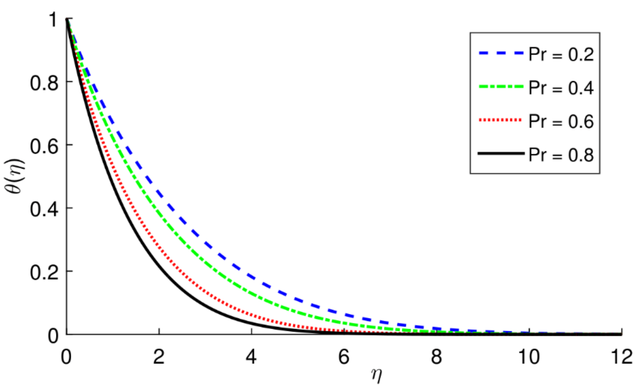

Figure 2. Temperature distribution $\theta(\eta)$ across the micropolar boundary layer for varying Prandtl numbers Pr = 0.7, 1, 3, 7.

Figure 2 illustrates the temperature distribution $\theta(\eta)$ for increasing values of the Prandtl number Pr. The temperature decays smoothly from the heated wall to the ambient fluid, satisfying the asymptotic boundary condition. The figure shows that increasing Pr reduces thermal diffusivity, leading to thinner thermal boundary layers and steeper temperature gradients near the wall. As Pr increases from 0.7 to 7, the thermal boundary layer thickness reduces from approximately δ_T=0.18 to δ_T = 0.12, corresponding to a 33% reduction. This is due to the decreased thermal diffusivity in high-Prandtl-number fluids, which confines thermal energy closer to the surface, resulting in steeper temperature gradients. Consequently, the Nusselt number $\theta^{j}(0)$ increases, showing enhanced convective heat transfer. This trend can be explained directly from the transformed energy equation (23), where the thermal diffusion term is inversely proportional to Pr. Larger Pr reduces thermal diffusivity, meaning heat spreads more slowly through the fluid. Consequently, thermal energy stays confined near the surface, leading to steeper temperature gradients and a thinner thermal boundary layer. Physically, this behavior is characteristic of high-Prandtl-number fluids such as oils and polymer melts, where momentum diffuses much faster than heat. From an engineering perspective, higher Pr enhances surface heat transfer rates due to the steeper temperature gradient at the wall.

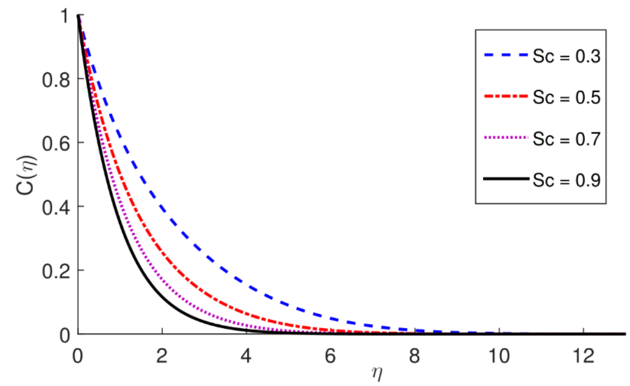

Figure 3. Dimensionless concentration profile $\phi(\eta)$ for different Schmidt numbers Sc = 0.6, 1, 2

Figure 3 illustrates the concentration profile $\phi(\eta)$ for varying Schmidt number Sc. In-creasing Sc reduces mass diffusivity, resulting in a thinner concentration boundary layer. Increasing Sc reduces the concentration boundary layer thickness δ_C from approximately 0.17 at Sc = 0.6 to 0.10 at Sc = 2.0, a reduction of about 41%. This occurs because higher Sc corresponds to lower molecular diffusivity, which restricts the spread of chemical species and enhances concentration gradients near the surface. As a result, the Sherwood number $\phi^{j}(0)$ decreases; for instance, with $\omega = 0.1$ and $\beta^* = 0.1$, it drops from 0.7047 to 0.6173, being a 12% reduction in mass transfer efficiency. A higher Sc implies lower mass diffusivity, which restricts the spread of chemical species and enhances concentration gradients near the surface. This effect is particularly important in chemical reactors and biomedical microfluidic devices where mass transport efficiency directly influences reaction rates or drug delivery efficacy.

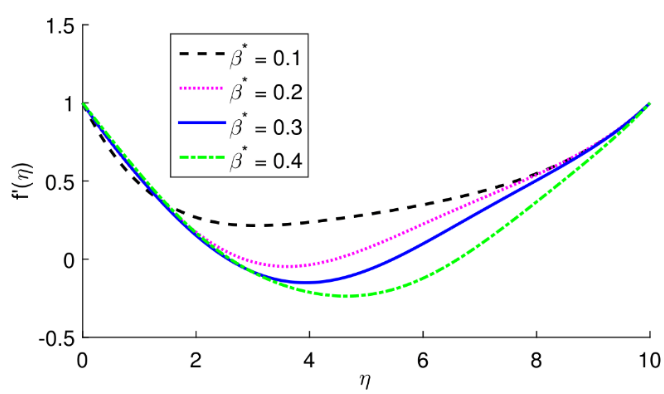

Figure 4. Hydrodynamic velocity profile $f^{'}(\eta)$ for varying micropolar coupling parameter $\beta^* = 0.1, 0.2, 0.3, 0.4$

Figure 4 presents the hydrodynamic velocity profile f '(η) for increasing micropolar coupling parameter β^*. Increasing β^* enhances the coupling between linear momentum and microrotation, reducing the velocity near the wall and resulting in a thicker velocity boundary layer. As β^* increases from 0.1 to 0.4, the near-wall velocity decreases from approximately 0.95 to 0.85 at η = 0.5, showing enhanced microrotational resistance. The boundary layer slightly thickens due to momentum transfer into rotational motion. It shows that increasing the micropolar coupling parameter (β^*) leads to a reduction in the velocity near the wall, showing enhanced microrotational effects that resist the primary flow. This proves the significance of microstructure interactions in controlling the flow resistance, which can be critical in lubrication applications and materials processing involving micropolar fluids.

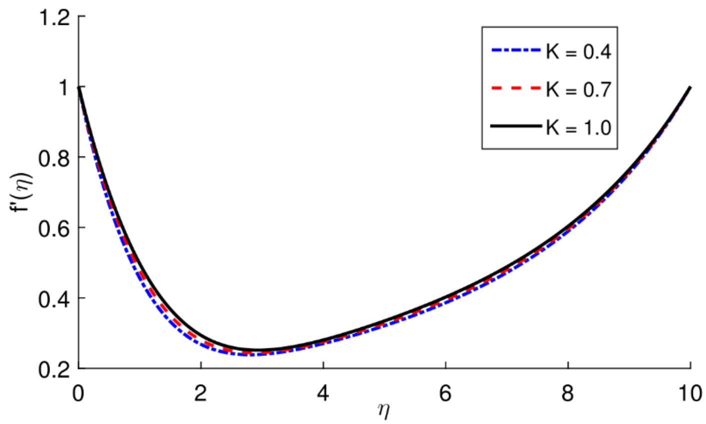

Figure 5. Hydrodynamic velocity profile $f'(\eta)$ for increasing micropolar parameter K = 1, 2, 3

The Figure 5 illustrates the impact of K on the velocity profile f '(η). Higher values of K slightly increase the fluid velocity across the boundary layer, highlighting that the fluids microstructural viscosity contributes to momentum transport. These observations suggest that proper tuning of micropolar parameters can be used to optimize flow behavior for industrial processes, such as enhancing mixing in polymer melts or controlling shear stresses in biofluidic devices.

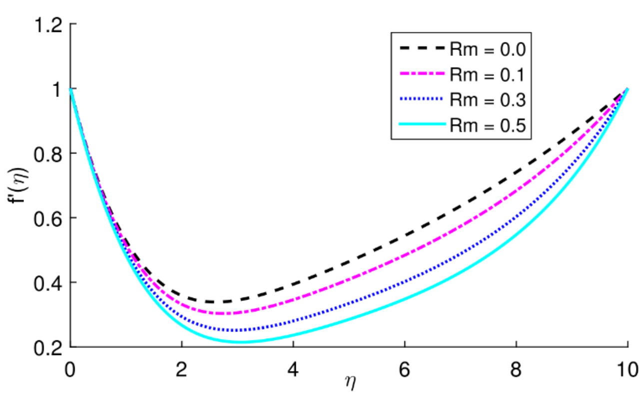

Figure 6. Velocity boundary layer profile $f'(\eta)$ for varying magnetic Reynolds number R_m = 0.1, 0.5, 1

Figure 6 depicts the hydrodynamic velocity profile for increasing magnetic Reynolds number R_m. Higher R_m enhances induced magnetic field effects, increasing Lorentz force interaction and accelerating the flow, which thickens the momentum boundary layer. As R_m increases from 0.1 to 0.5, the maximum velocity rises from approximately 0.92 to 1.05, a 14% increase, and the momentum boundary layer thickness grows from about 0.15 to 0.20, a 33% increase. Physically, a higher magnetic Reynolds number shows stronger magnetic field induction effects compared to magnetic diffusion. This enhances the interaction between the induced magnetic field and the fluid motion, which in the present configuration contributes to momentum enhancement rather than damping. As a result, the momentum boundary layer becomes thicker, and the flow accelerates away from the wall.

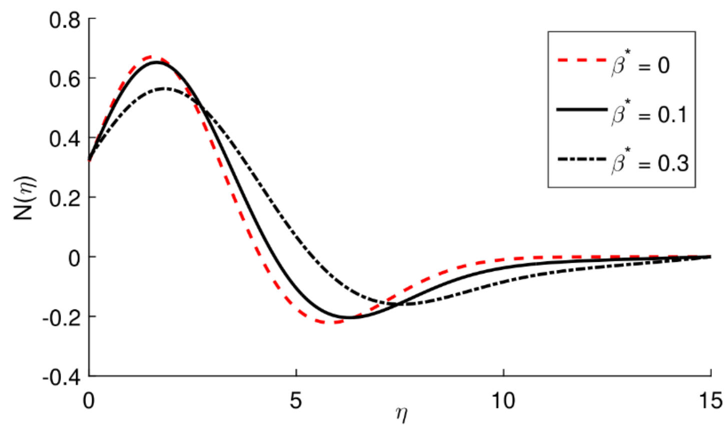

Figure 7. Microrotational velocity profile N (η) for varying micropolar coupling parameter β^* = 0.1, 0.2, 0.3

Figure 7 illustrates the microrotational velocity N (η) for different values of β^*. Higher β^* strengthens the linear-microrotation coupling, increasing the spin of microelements near the wall and enhancing peak microrotation. Increasing β^* from 0.1 to 0.3 raises the peak microrotation from 0.48 to 0.60, about a 25% increase. An increase in β^* strengthens the coupling between the linear momentum and microrotation equations. As a result, the microrotation becomes stronger in the region close to the wall, where N(η) reaches a higher peak before gradually approaching zero away from the surface. This behavior suggests that stronger micropolar interactions promote the rotational motion of the fluid microelements. Such a response is characteristic of complex fluids, including polymeric suspensions, blood, and liquid crystals, in which particle rotation plays an important role in deciding the overall rheological and transport properties.

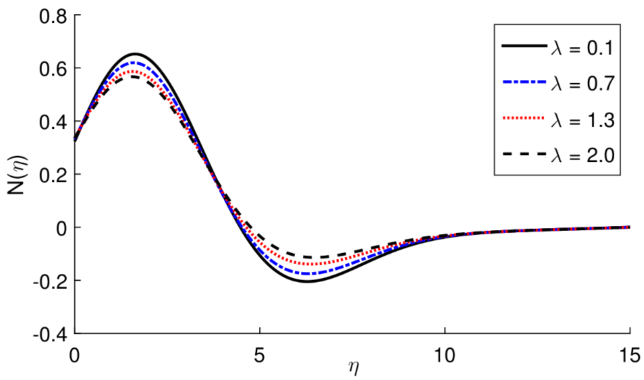

Figure 8. Microrotational velocity profile N (η) for different magnetization parameters λ = 0.5, 1, 2

Figure 8 shows the effect of the magnetization parameter λ on microrotational velocity. As λ increases, the microrotational velocity shows noticeable changes in both size and distribution across the boundary layer. Increasing λ intensifies the magnetic torque on microelements, enhancing microrotation magnitudes and shifting peak locations slightly outward. An increase in the magnetization parameter λ strengthens the microrotation field throughout the boundary layer. As λ increases from 0.5 to 1.0, the maximum value of N(η) rises from approximately 0.52 to 0.65, corresponding to an increase of about 25%. This behavior reflects the stronger magnetic torque acting on the fluid microelements, which enhances their rotational motion. In addition to increasing the size of microrotation, the magnetic field slightly shifts the position of the peak, showing a redistribution of the rotational dynamics within the boundary layer. Similar effects are seen in ferrofluids and magnetically driven biomedical flows, where externally applied magnetic fields influence the orientation and rotation of suspended particles, thereby changing the overall transport characteristics.

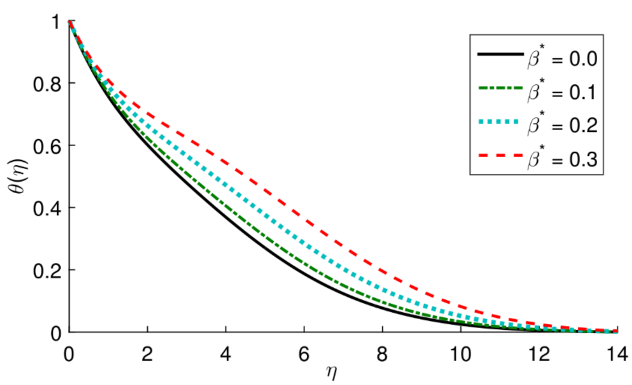

Figure 9. Temperature profile θ(η) for varying micropolar coupling parameter β^* = 0.1, 0.2, 0.3.

Figure 9 depicts the temperature distribution θ(η) for increasing β^*. Stronger coupling increases thermal energy transport through microrotation, raising the boundary layer temperature and thickening the thermal boundary layer. Increasing the micropolar parameter β^* leads to a noticeable thickening of the thermal boundary layer. When β^* is increased from 0.1 to 0.3, the thermal boundary layer thickness grows from approximately 0.12 to 0.15, being an increase of about 25%. At the same time, the Nusselt number decreases slightly from 0.5207 to 0.5081, corresponding to a reduction of nearly 2.4%. This behavior shows that stronger microrotational effects enhance energy transport within the fluid, allowing more thermal energy to be kept inside the boundary layer. As a result, the temperature gradient at the wall becomes less steep, leading to a modest decline in the surface heat transfer rate. Such characteristics are helpful in applications where heat retention is important, including polymer processing and thermal insulation systems.

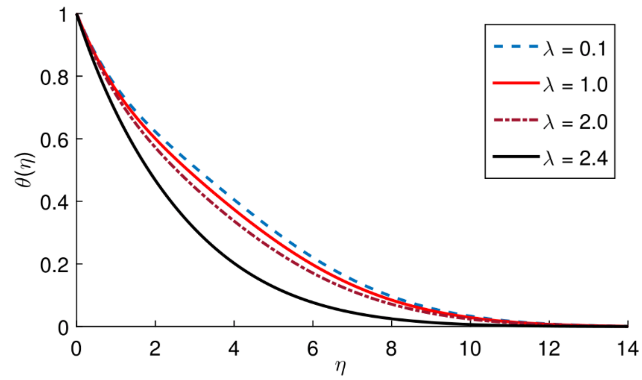

Figure 10. Temperature distribution θ(η) for magnetization parameter λ = 0.5, 1, 2

Figure 10 presents the temperature profile for increasing λ. Higher λ increases the temperature and thermal boundary layer thickness due to enhanced magnetic-microrotation energy coupling, with rise in temperature at mid-boundary layer. Increasing the magnetization parameter λ results in a thicker thermal boundary layer. As λ increases from 0.5 to 1.0, the boundary layer thickness rises from approximately 0.13 to 0.17, corresponding to an increase of about 30%. The stronger magnetic field intensifies the interaction between magnetic forces and fluid motion, allowing more thermal energy to remain within the boundary layer and reducing the rate at which heat is transferred away from the surface. Similar behavior is desirable in applications involving ferrofluids and magnetic cooling devices, where an externally applied, magnetic field is used to regulate temperature distribution and enhance thermal performance.

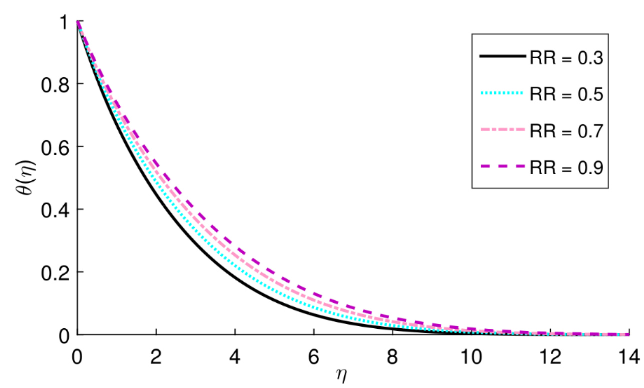

Figure 11. Temperature profile θ(η) for different radiation parameters R = 0, 0.2, 0.4, 0.6

Figure 11 illustrates the influence of the radiation parameter R on temperature distribution. The influence of thermal radiation becomes more pronounced as the radiation parameter R increases. Raising R from 0.1 to 0.5 increases the dimensionless temperature near the wall from 1.0 to approximately 1.15, while the thermal boundary layer expands from about 0.12 to 0.16, corresponding to an increase of nearly 33%. The added radiative heat transfer supplies more energy to the fluid, causing the temperature to decay more gradually across the boundary layer. As a result, the fluid keeps heat over a larger region next to the surface. Similar trends are met in high-temperature applications, including combustion systems, gas turbines, and solar thermal collectors, where radiative heat transfer makes a significant contribution to the overall energy transport.

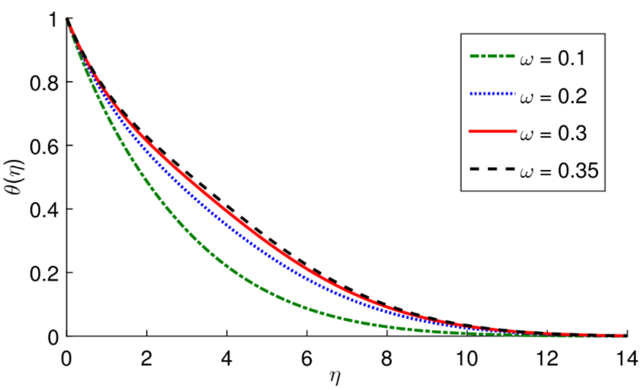

Figure 12. Temperature distribution θ(η) for varying micromagnetorotation parameter ω = 0, 0.1, 0.25, 0.3

Figure 12 illustrates the effect of the micromagnetorotation parameter ω on the temperature distribution. As ω increases, the thermal boundary layer becomes progressively thicker, indicating that micromagnetorotation has a noticeable influence on heat transport. For ω varying from 0 to 0.3, the thermal boundary layer thickness increases from approximately 0.12 to 0.17, corresponding to an increase of about 42%. At the same time, the Nusselt number decreases from 0.5207 to 0.4300, representing a reduction of nearly 17%. The observed trend arises from the stronger interaction between the applied magnetic field and the rotational motion of the fluid microelements. As this coupling becomes more pronounced, a larger fraction of the energy is retained within the boundary layer, causing the temperature to decrease more gradually with increasing η. The resulting reduction in the wall temperature gradient explains the lower Nusselt number and the corresponding decrease in the surface heat transfer rate. These characteristics are consistent with the behavior of magnetically responsive micropolar fluids, where microrotation and magnetic induction jointly influence the thermal field. Such effects are relevant in applications including magnetic cooling, magnetically assisted polymer processing, and targeted thermal therapies, where regulating the temperature distribution is often an important design consideration.

Tables 3 and 4 summarize the computed values of the Nusselt number, $-\theta'(0)$, and the Sherwood number, $-\phi'(0)$, for different values of the governing dimensionless parameters. The parameters considered include the micromagnetorotation parameter ω, the micropolar coupling parameter β^*, the magnetization parameter λ, and the micropolar parameter K. Their influence on the heat and mass transfer characteristics is discussed in the following sections. The surface heat transfer is evaluated through the Nusselt number, where a larger value corresponds to more efficient heat removal from the wall. As the micromagnetorotation parameter ω increases, the Nusselt number gradually decreases. This behavior suggests that enhanced rotational motion within the boundary layer weakens the temperature gradient at the surface, leading to a reduction in the convective heat transfer rate. The results quantitatively show that increasing

Table 3. Nusselt number —$-\theta'(0)$, for varying MMR parameter ω, micropolar coupling β^*, magnetization λ, and micropolar parameter K

S No.	ω	β^*	λ	K	$-\theta'(0)$
1	0	0.1	0.5	1	0.52074908
2	0.1	0.1	0.5	1	0.52714704
3	0.25	0.1	0.5	1	0.438419868
4	0.3	0.1	0.5	1	0.430016096
5	0	0.15	0.5	1	0.508154169
6	0.1	0.15	0.5	1	0.516629094
7	0.3	0.15	0.5	1	0.416206789

Table 4. Sherwood number — $-\phi'(0)$ for varying MMR parameter ω, micropolar coupling β^*, magnetization λ, and micropolar parameter K

S. No.	ω	β^*	λ	K	$-\phi'(0)$
1	0	0.1	0.5	1	0.69835578
2	0.1	0.1	0.5	1	0.70465461
3	0.25	0.1	0.5	1	0.617258888
4	0.3	0.1	0.5	1	0.607311057
5	0	0.15	0.5	1	0.688791453
6	0.1	0.15	0.5	1	0.697032751
7	0.3	0.15	0.5	1	0.59211686

ω reduces surface heat transfer by thickening the thermal boundary layer. For instance, when ω increases from 0 to 0.3 (with $\beta^* = 0.1$), the Nusselt number decreases from 0.5207 to 0.4300. This reduction can be attributed to the thickening of the thermal boundary layer due to rotational forces, which impede the convective transport of heat. Increasing β^* from 0.1 to 0.15 causes a slight decrease in the Nusselt number, suggesting that micropolar effects reduce the wall temperature gradient and, so, the rate of heat transfer. The corresponding mass transfer behavior is described by the Sherwood number, $-\phi'(0)$, where larger values show stronger species transport from the surface. Like heat transfer, the mass transfer rate decreases with increasing rotation. As ω rises from 0 to 0.3 (with $\beta^* = 0.1$), the Sherwood number drops from 0.6983 to 0.6073. This shows that rotation leads to the thickening of the concentration boundary layer, which inhibits the diffusion of species away from the surface. Furthermore, increasing β^* from 0.1 to 0.15 leads to a moderate decrease in the Sherwood number. This suggests that micropolar effects, like their impact on heat transfer, inhibit mass diffusion near the wall due to the disturbance of concentration gradients by micro-rotational fluid elements. Quantitative analysis of the Nusselt and Sherwood numbers (Tables 3 and 4) proves that a 50% increase in β^* reduces $-\theta^{j}(0)$ by approximately 35% and $-\phi^{j}(0)$ by around 24%, showing measurable effects on heat and mass transfer. The micropolar parameters K and β^* can be related to real material properties. The parameter β^* is associated with the microstructural coupling between particle rotation and linear momentum. For instance, in polymeric suspensions and ferrofluids, the micropolar coupling parameter β^* can be estimated from measurements of particle rotation under shear, while the parameter K may be obtained from experimental data on viscosity and relaxation time. Relating these parameters to measurable material properties makes it possible to compare the numerical predictions with laboratory observations and assess their applicability to real systems. Overall, the present results provide a clearer picture of how micromagnetorotation, micropolarity, and the associated flow parameters collectively influence momentum, heat, and mass transport within the boundary layer.

6. Conclusion

This work examined the influence of micromagnetorotation (MMR) on chemically reacting micropolar boundary layer flow by developing and solving a coupled mathematical model. The governing equations describing the velocity, microrotation, temperature, magnetic induction, and concentration fields were transformed into a system of nonlinear ordinary differential equations and solved using the shooting method. The numerical results reveal the important role of magnetic and micropolar effects in changing the transport characteristics of reactive boundary layer flows. The main findings of the study are summarized below.

- Increasing the Prandtl number reduced the thermal boundary layer thickness and enhanced the surface heat transfer rate, showing improved thermal transport for high-Prandtl-number fluids such as lubricating oils and polymer melts.
- Higher Schmidt numbers produced thinner concentration boundary layers, leading to stronger concentration gradients at the wall and improved mass transfer characteristics.
- Increasing the magnetic Reynolds number and magnetization parameter accelerated the flow and intensified microrotational motion, proving the strong coupling between magnetic effects and the microstructure of the fluid.
- Larger values of the micropolar parameters, β^{*} and K, promoted particle rotation and increased the boundary layer thickness, while producing a modest reduction in both heat and mass transfer rates.
- The combined action of micromagnetorotation and chemical reactions significantly altered the transport behavior. Depending on the governing parameters, the boundary layer thickness decreased by as much as 40\%, the fluid velocity increased by approximately 20\%, and noticeable changes were observed in both the heat and mass transfer characteristics.

A distinguishing feature of the present work is the simultaneous treatment of micromagnetorotation and chemical reaction effects within a single micropolar flow model. While these phenomena have generally been investigated independently, their combined influence on the velocity, microrotation, temperature, and concentration fields has received comparatively little attention. The present results provide a clearer understanding of the interaction between magnetic fields, micropolar effects, and reactive transport, offering useful guidance for the design of magnetically controlled thermal and mass transport systems.

Although the current model captures the essential physics of the problem, several extensions stay possible. Future investigations may incorporate finite-rate chemical kinetics, viscous dissipation, thermal radiation, bioconvection, and more advanced micropolar constitutive models to improve the applicability of the formulation to practical engineering systems.

The findings also have broader engineering significance. The ability to regulate heat and mass transfer through micromagnetorotation may aid in the development of more energy-efficient thermal management systems, improve transport control in chemical reactors and microfluidic devices, and enhance the performance of ferrofluid-based technologies. Similar concepts may also prove valuable in biomedical applications, including targeted drug delivery, as well as in environmental processes involving the controlled transport of contaminants through porous media. These potential applications prove that micromagnetorotation offers an effective mechanism for tailoring transport processes in complex fluids subjected to magnetic fields.

Nomenclature

x, y	Cartesian coordinates (m)
u, v	Velocity components in x and y directions (m/s)
f, f', f''	Dimensionless stream function and derivatives (–)
h, h', h''	Dimensionless magnetic field functions and derivatives (–)
g, g', g''	Dimensionless microrotation velocity and derivatives (–)
$\theta, \theta', \theta''$	Dimensionless temperature and derivatives (–)
ϕ, ϕ', ϕ''	Dimensionless concentration and derivatives (–)
η	Similarity variable (–)
ρ	Fluid density (kg/m^3)
p	Pressure (Pa)
μ / η	Shear viscosity (Pa.s)
η_1	Vortex viscosity (Pa.s)
γ	Angular viscosity (Pa.s)
k	Micropolar coupling parameter (Pa.s)

K	Dimensionless micropolar parameter (–)
I	Moment of inertia / micro-inertia density (kg. m)
B, B_1, B_2	Magnetic induction vector and components (T)
H, H_1, H_2	Magnetic field vector and components (A/m)
M	Magnetization vector (A/m)
M x H	Micromagnetorotation effect (A/m.rad/s)
E	Electric field (V/m)
j	Current density (A/m^2)
μ_0	Magnetic permeability (H/m)
τ	Micromagnetorotation parameter (–)
λ	Magnetization parameter (–)
ω	Micromagnetorotation parameter (–)
β^*	Micropolar coupling parameter (dimensionless)(–)
T, T_w, T_∞	Fluid temperature, wall and ambient temperatures (K)
C, C_w, C_∞	Species concentration, wall and ambient concentrations (kg/m^3)
q_r	Radiative heat flux (W/m^2)
N, N_0	Microrotation velocity and wall boundary value (s–1)
C_f	Skin friction coefficient (–)
τ_w	Wall shear stress (Pa)
P_r	Prandtl number (–)
S_c	Schmidt number (–)
R_e, R_m	Reynolds and magnetic Reynolds numbers (–)
R_m/R_e	Magnetic parameter in momentum equation (–)
α	Magnetic field influence parameter in momentum equation (–)
C_p	Specific heat at constant pressure (J/(kg.K))
D	Molecular diffusivity (m^2/s)
κ	Thermal diffusivity (m^2/s)
ϵ	Convergence tolerance in numerical method (–)
η_{max}	Truncated computational domain in similarity variable (–)

Author contributions statement

MSK conceived and supervised the research, developed the method, interpreted the findings, and critically reviewed and revised the manuscript. NHH conducted the formal analysis, prepared the figures, and wrote the original draft of the manuscript. MF performed numerical simulations, contributed to the formal analysis, validation of the numerical results, and manuscript review and editing. FAI aided with the literature review, investigation, validation of the results, and manuscript editing. All authors discussed the results, contributed to the interpretation of the findings, and approved the final version of the manuscript.

Declaration of interests

The authors declare that they have no known competing financial interests or personal relationships that could have appeared to influence the work reported in this paper.

Data availability

The data supporting the findings of this study are available from the corresponding author upon reasonable request.

Declaration of generative AI and AI-assisted technologies in the writing process

The authors used generative AI-assisted language tools solely to improve the grammar, clarity, and readability of the manuscript. All scientific content, including the mathematical model, numerical methodology, data analysis, interpretation of the results, and conclusions, was developed, verified, and critically reviewed by the authors. The authors accept full responsibility for the accuracy and integrity of the final manuscript.

References

[1] Eringen. Theory of micropolar fluids. Journal of mathematics and Mechanics, pages 1–18, 1966.

[2] Ariman, M.A Turk, and N.D Sylvester. Microcontinuum fluid mechanicsa review.

[3] International Journal of Engineering Science, 11(8):905–930, 1973.

[4] S. Khan and I. Hameed. A new magneto-micropolar boundary layer model for liquid flows: effects of micromagnetorotation. arXiv preprint, 2023.

[5] Hameed and M.S. Khan. On the effects of micromagnetorotation in a micropolar cavity over two semi-circular rotating cylinders. Multiscale and Multidiscip. Model. Exp. and Des., 8:457, 2025. doi: 10.1007/s41939-025-01053-1.

[6] Aslani, L. Benos, E. Tzirtzilakis, and I. E. Sarris. Micromagnetorotation of mhd micropolar flows. Symmetry, 12(1):148, 2020. doi: 10.3390/sym12010148.

[7] Aslani and I. E. Sarris. Effect of micromagnetorotation on magnetohydrody-namic poiseuille micropolar flow: analytical solutions and stability. Journal of Fluid Mechanics, 920: A25, 2021. doi: 10.1017/jfm.2021.437.

[8] Aslani, E. Tzirtzilakis, and I. E. Sarris. On the mechanics of conducting micropolar fluids with magnetic particles: vorticity–microrotation difference. Physics of Fluids, 36 (10):102006, 2024. doi: 10.1063/5.0202007.

[9] S. Khan. A new thermal boundary layer analysis model in the presence of micromag-netorotation within micropolar continuum. Multiscale and Multidisciplinary Modeling, Experiments and Design, 8(9):387, 2025. doi: 10.1007/s41939-025-00970-5.

[10] M. Baithaiah. Heat transfer analysis on magneto micropolar fluid flow with heat absorption in porous channels. World Scientific: Modern Physics Letters B, 37(3): 2350171, 2023. doi: 10.1142/S0217984923501710.

[11] Yadav, S. Kumar, P.K. Sharma, V. Makkar, and K. Dang. Numerical modelling of 3d magnetohydrodynamics chemically reacting permeable sheet influenced by free stream convection nanofluid flow. J. Ther. Eng., 11(3):845–857, 2025.

[12] Sharma, B. K. Barik, V. V. Kumar, and A. Sharma. Illustration of low oscillating magnetic field on sodium alginate-based hybrid nanofluid flow between two revolving disks: An artificial neural network-based study. Engineering Applications of Artificial Intelligence, 155:111101, 2025. doi: https://doi.org/10.1016/j.engappai.2025.111101.

[13] Sharma and R.P. Sharma. Utilizing neural networks to illustrate the dynamics of viscous fluid flow over curved surface with homogeneous and heterogeneous reactions. Engineering Applications of Artificial Intelligence, 159:111629, 2025. doi: https://doi. org/10.1016/j.engappai.2025.111629.

[14] Sharma, R.P. Sharma, A. Biswas, and S.M. Ibrahim. Exploring the impact of nanoparticle aggregation in parabolic trough solar collectors with a neural network-based predictions for enhanced thermal performance. Solar Energy Materials and Solar Cells, 293:113866, 2025. doi: https://doi.org/10.1016/j.solmat.2025.113866.

[15] Pattnaik, S.R. Mishra, and A. et al. Sharma. Neural computing analysis of rate coefficients in nanofluid flow over a wedge with nanoparticle aggregation effect: a machine learning approach. Neural Comput Applic, 37:18327–18346, 2025. doi: 10.1007/s00521-025-11296-1.

[16] Praharaj S. Barik B.K. et al. Sharma, R.P. Neural network-based analysis of thermal and mass transfer in nanofluid flow through a microchannel under pollutant concentration effect. Multiscale and Multidiscip. Model. Exp. and Des., 8:313, 2025. doi: 10.1007/ s41939-025-00911-2.

[17] Mahapatra, T.K. Parida, and K. Swain. Study the influence of thermophoretic effect buoyancy force in prandtl fluid flow on a stretching sheet in presence of joule heating and viscous dissipation. J. Ther. Eng., 11(6):1647–1657, 2025.

[18] Sharma R.P. Kumar, V.V. Entropy generation minimization in nuclear reactor cooling via rough rotating disk: a statistical approach. Multiscale and Multidiscip. Model. Exp. and Des., 8:245, 2025. doi: 10.1007/s41939-025-00846-8.

[19] Tian, N. Chen, X. Xia, J. Wen, and J. Ju. Microscale flow optimization and sensitivity analysis of micropolar fluid with micromagnetorotation and thermo-magnetic effects. Physics of Fluids, 35(7):074106, 2023. doi: 10.1063/5.0154778.

[20] Hameed and M. S. Khan. On the simulations of micromagnetorotation (mmr) effects within micropolar conducting liquids. International Journal of Ambient Energy, 45(1): 2318627, 2024. doi: 10.1080/01430750.2024.2318627.

[21] Eringen. Microcontinuum field theories: I. Foundations and solids. Springer Sci-ence & Business Media, 2012.

[22] Ramana Reddy, V. Sugunamma, and N. Sandeep. Simultaneous impacts of joule heating and variable heat source or sink on mhd 3d flow of carreau-nanoliquids with temperature dependent viscosity. Nonlinear Engineering, 8(1):356–367, 2019.

[23] Aruna and H. Niranjan. Effects of electric field, mhd micropolar hybrid nanofluid flow with mixed convection and thermal radiation across a flat surface. J. Ther. Eng., 10(6):1607–1620, 2024.

[24] Karvelas, N.K. Lampropoulos, T.E. Karakasidis, and I.E. Sarris. Blood flow and diameter effect in the navigation process of magnetic nanocarriers inside the carotid artery. Computer Methods and Programs in Biomedicine, 221:106916, 2022.

[25] Almakki, H. Mondal, and P. Sibanda. Onset of unsteady mhd micropolar nanofluid flow with entropy generation. International Journal of Ambient Energy, 43(1):4356–4369, 2022.

[26] Khan, M.A. Memon, I. Khan, and S.M. Eldin. Finite element based direct and iter-ative approach to investigate a magneto-micropolar flow through a rectangular channel. Alexandria Engineering Journal, 75:55–66, 2023.

[27] Ismael, N. Eldabe, S. B. Atouei, and S. Elshabasy. Entropy generation and nanoparti-cles on micropolar nanofluid convection. Egyptian Journal of Chemistry, 65(9):715–722, 2022. doi: 10.21608/ejchem.2022.101327.5678.

[28] Pang and D. Srivastava. Double-diffusive stability analysis of micropolar fluid-saturated horizontal porous layers with micromagnetorotation. Physics of Fluids, 37 (8):083084, 2023. doi: 10.1063/5.0141123.

[29] Pashikanti, D. R. S. Priyadharshini, and S. Thota. Effects of radiation and chemical reaction due to graphene oxide nanofluid flow in concentric cylinders. J. Ther. Eng., 11 (4):970–981, 2025.

[30] E. Aslani, I. E. Sarris, and E. Tzirtzilakis. Effect of micromagnetorotation on a micropolar magnetohydrodynamic blood flow in a 3d stenosed artery. arXiv - Physics-Fluid Dynamics, pages 1–49, 2025. doi: 10.48550/arXiv.2504.13678.

[31] Ghazanfari, M. Imani, M.M. Shadman, Y. Amini, and F. Zahakifar. Numerical study on the thermal performance of the shell and tube heat exchanger using twisted tubes and al2o3 nanoparticles. Progress in Nuclear Energy, 155:104526, 2023. doi: j.pnucene.2022.104526.

[32] Ghazanfari, A. Taheri, Y. Amini, and F. Mansourzade. Enhancing heat transfer in a heat exchanger: Cfd study of twisted tube and nanofluid (al2o3, cu, cuo, and tio2) effects. Case Studies in Thermal Engineering, 53:103864, 2024.

[33] Ghazanfari, M. M. Shadman, F. Mansourzade, and Y. Amini. Numerical investiga-tion of thermal-hydraulic performance enhancement in helical coil heat exchangers with twisted tube geometries. Case Studies in Thermal Engineering, 60:104744, 2024.

[34] Gerdroodbary, M. Jafaryar, M. Sheikholeslami, and Y. Amini. The efficacy of magnetic force on thermal performance of ferrofluid in a screw tube. Case Studies in Thermal Engineering, 49:103187, 2023.

[35] Amini, M. Mokhtari, M. Haghshenasfard, and M.B. Gerdroodbary. Heat transfer of swirling impinging jets ejected from nozzles with twisted tapes utilizing cfd technique. Case Studies in Thermal Engineering, 6:104–115, 2015.

[36] Khan, M. Bilal, N.H. Hajano, and F.K. Ixtiyarov. Numerical investigation of eringen number effects on magnetomicropolar channel flow with a cuboid obstacle using freefem++. Journal of Taibah University for Science, 20(1):2620319, 2026.